Vol. 81, No. 20

The Structure of a Putative Scaffolding Protein of Immature Poxvirus Particles as Determined by Electron Microscopy Suggests Similarity with Capsid Proteins of Large Icosahedral DNA Viruses[∇]

Jae-Kyung Hyun,[1]† Fasséli Coulibaly,[1]† Adrian P. Turner,[1] Edward N. Baker,[1]
Andrew A. Mercer,[2] and Alok K. Mitra[1]*

*School of Biological Sciences, University of Auckland, Postal Bag 92019, Auckland, New Zealand,[1] and Department of
Microbiology and Immunology, University of Otago, Post Office Box 56, Dunedin, New Zealand[2]*

Orf virus, the prototype parapoxvirus, is responsible for contagious ecthyma in sheep and goats. The central region of the viral genome codes for proteins highly conserved among vertebrate poxviruses and which are frequently essential for viral proliferation. Analysis of the recently published genome sequence of orf virus revealed that among such essential proteins, the protein orfv075 is an orthologue of D13, the rifampin resistance gene product critical for vaccinia virus morphogenesis. Previous studies showed that D13, arranged as "spicules," is necessary for the formation of vaccinia virus immature virions, a mandatory intermediate in viral maturation. We have determined the three-dimensional structure of recombinant orfv075 at ~25-Å resolution by electron microscopy of two-dimensional crystals. orfv075 organizes as trimers with a tripod-like main body and a propeller-like smaller domain. The molecular envelope of orfv075 shows unexpectedly good agreement to that of a distant homologue, VP54, the major capsid protein of *Paramecium bursaria Chlorella* virus type 1. Our structural analysis suggests that orfv075 belongs in the double-barreled capsid protein family found in many double-stranded DNA icosahedral viruses and supports the hypothesis that the nonicosahedral poxviruses and the large icosahedral DNA viruses are evolutionarily related.

Orf virus (ORFV) is the prototype parapoxvirus, infecting sheep and goats worldwide. It is responsible for contagious ecthyma, also known as soremouth or orf, characterized by the progressive development of erythema, pustules, and scab usually around the mouth and nostrils of young animals (18). This may result in an inability to suckle and subsequent failure to thrive. The virus also readily infects humans, where similar skin lesions develop, most frequently on the hands. Interestingly, ORFV is capable of infecting the same host repeatedly in the presence of a normal host immune response, most likely because of species-specific virulence and immunomodulatory factors encoded by the terminal regions of the viral genome (17). By contrast with the variable ends of the genome, the central region is widely conserved among vertebrate poxviruses and encodes proteins essential to the viral replication and assembly (14, 18).

Poxviruses are large, double-stranded DNA viruses which replicate and assemble inside the cytoplasm of infected cells (34). These viruses are characterized by a complex virion morphology, described as brick shaped or ovoid with surface decoration of tubule structures (20). These tubular structures adopt a characteristic criss-cross pattern in parapoxviruses, suggesting a helical arrangement on the surface of virions (46). Poxviruses undergo a complex maturation process with several distinct viral assembly intermediates that have been described

in detail by electron microscopy (EM) studies of vaccinia virus (10). Viral maturation initiates with the condensation of viral proteins and genetic material in an area called the "viral factory," which appears as an uniformly dense region surrounded by membranous organelles within the host cytoplasm (48). Crescent-shaped membranes decorated with protein spicules on their convex surface then form around the viral factory (13). The crescents subsequently wrap into spherical structures termed immature virions (IV) which contain the viral core proteins and the genome (40, 44). The transition between these IV and intracellular mature virions (IMV) involves a major morphological change from spherical to brick-shaped virions. IMV exhibit a more complex structure consisting of an outer membrane, a biconcave core, and two lateral bodies filling the cavities as well as a coiled DNA-protein complex confined in the core wall (12, 20, 28). Such dramatic morphological changes result from a complex rearrangement involving the proteolytic processing of viral core proteins (8, 24, 31, 41). The virus particles then wrap into membranes of the host trans-Golgi network to form intracellular enveloped virions. These finally fuse with the cell membrane and exit the host cytoplasm as extracellular enveloped virions (27, 43). We note that recently an alternate nomenclature has been proposed in which the terms mature virion, wrapped virion, and extracellular virion have been used for IMV, intracellular enveloped virion, and extracellular enveloped virion, respectively (10, 35). In what follows we have used the "classical" nomenclature.

The spicules found on the crescent-shaped membranes of IV are formed by a viral protein called D13 (32, 33). This protein is also the target of rifampin (5, 29, 37). The presence of this antibiotic reversibly inhibits the localization of D13 on IV and stops viral assembly (36). In addition, abrogation of D13 ex-

pression results in aberrant IV formation, similar to the effect of rifampin (50). More recent studies show that trimers of D13 arrange in a "honeycomb lattice" on the vaccinia virus IV surface (20, 47). While D13 appears to have a crucial role in the formation of IV, it is lost in the IV-to-IMV transition and cannot be detected in infectious forms of vaccinia virus virions (15, 44). How the protein interacts with membranes and what causes the removal of spicules during the IMV formation are poorly understood. D13 orthologues are found in all members of the poxvirus family, with a high degree of sequence conservation. In addition, D13 shares conserved domains with the coat proteins found in distant homologues that belong in the group called nucleocytoplasmic large DNA viruses (NCLDV) (21, 22).

In ORFV, the orfv075 protein was identified as the vaccinia virus D13 orthologue, with 57% sequence identity (14). We have investigated the structure of orfv075, with the ultimate goal of understanding its possible contribution to ORFV morphogenesis. We have determined the three-dimensional (3-D) structure of orfv075 at 25-Å resolution by EM of 2-D crystals. orfv075 organizes as a trimer, and the 3-D model reveals that the trimer is barrel shaped with a tripod-like base on one end and a smaller propeller domain on the other end. The 3-D model of orfv075 indicates a structural similarity with capsid proteins of the large icosahedral DNA viruses and suggests the presence of two consecutive jelly roll domains that are oriented parallel to each other, resulting in a pseudohexameric trimer. Our results suggest that orfv075 belongs in the double-barrel capsid protein family, characteristic of an ancient viral lineage spanning all domains of life (6, 26). This lineage was defined based on structural studies of double-stranded DNA icosahedral viruses, and poxvirus could be the first member of this family with an infectious virion lacking icosahedral symmetry.

MATERIALS AND METHODS

Expression and purification. The *orfv075* gene was amplified by PCR from genomic DNA of the NZ2 strain of ORFV. BamHI and HindIII restriction sites were introduced in the forward and reverse PCR primers, respectively, for cloning in a pPROEX Hta (Invitrogen) vector with an amino-terminal His$_6$ tag (His tag), followed by a cleavage site for the recombinant tobacco etch virus (rTEV) N1a protease. Expression of the orfv75 protein in BL21 pRP *Escherichia coli* was induced by addition of 0.5 mM IPTG (isopropyl-β-D-thiogalactopyranoside) at an optical density at 600 nm of 1.0, and cells were grown for 12 to 15 h at 18°C. The cell culture was centrifuged at 3,000 × *g* for 30 min at 4°C in an SLC-4000 rotor (Sorvall). The cell pellet was resuspended in 10 ml of cold lysis buffer (50 mM Tris-HCl [pH 8.0], 300 mM NaCl, 20% glycerol, 5 mM β-mercaptoethanol, one EDTA-free protease inhibitor tablet [Roche] and 0.1 mg/ml lysozyme). Cells were then mechanically disrupted in a One-Shot cell disruptor (Constant System) at 18 kPa. The lysate was centrifuged at 30,000 × *g* at 4°C in an SS-34 rotor (Sorvall) for 30 min, and the supernatant was subjected to immobilized metal affinity chromatography using a 5-ml Ni-nitrilotriacetic acid column (HiTrap Chelating HP; Amersham Biosciences). Washes with buffer (20 mM phosphate buffer [pH 7.2] and 500 mM NaCl) containing 50 and 150 mM imidazole removed most of the contaminants, and orfv075 was eluted with 500 mM imidazole. Further purification was carried out by size exclusion chromatography (SEC) using a Superdex HR 200 10/30 column on a fast protein liquid chromatography system (Amersham Biosciences), wherein the protein was finally purified in 50 mM Tris-HCl (pH 8.0), 150 mM NaCl, 2 mM β-mercaptoethanol. Estimation of the molecular mass of purified His tag-cleaved orfv075 oligomer was carried out by plotting log values of molecular masses of standards as a function of distribution coefficients (4).

2-D crystallization in situ. His-tagged orfv075 protein, when changed from 50 mM to 10 mM Tris buffer, led to 2-D crystallization. A 200-μg/ml concentration of protein in 50 mM Tris, 150 mM NaCl (pH 8.0) was diluted 10-fold in 10 mM Tris, 200 mM NaCl (pH 8.0) and then concentrated back to the initial volume

using a 30,000-Da molecular mass cutoff Vivaspin500 (Vivascience) by centrifugation at 11,000 × *g* at 4°C. The dilution/concentration procedure was repeated three times. Examination of the final concentrated sample by EM showed the presence of 2-D crystals. Hereafter, these crystals are referred to as type I crystals.

2-D crystallization on lipid monolayer. A mixture of egg L-α-phosphatidylcholine and egg phosphatidyl-DL-glycerol at a 2:1 (wt/wt) ratio was doped with nickel-chelating lipid DOGS {1,2-dioleoyl-*sn*-glycero-3-[(*N*-(5-amino-1-carboxypentyl)iminodiacetic acid)succinyl]}-nitrilotriacetic acid-Ni (nickel salt) in 3:1 (wt/wt) ratio in 80% chloroform and 20% methanol. All lipids were obtained from Avanti Polar Lipids. One microliter of the lipid solution was layered onto the surface of 35 μl of 50 mM, Tris pH 8.0, containing 150 mM NaCl and 50 mM imidazole in a 4-mm-wide and 4-mm-deep Teflon well as described by Lévy et al. (27). The lipid monolayer was allowed to form following complete evaporation of the organic solvent. Recombinant His-tagged orfv075 in 50 mM Tris, pH 8.0, containing 150 mM NaCl and 50 mM imidazole was then injected through a port at the bottom of the well at a final protein concentration of 50 μg/ml. After 3 h of undisturbed incubation at room temperature, the monolayer at the air-water interface containing 2-D crystals was transferred onto a hydrophobic EM grid covered with holey carbon support film (Quantifoil, R2/2). Hereafter, these crystals are referred to as type II crystals.

Transmission EM of purified protein samples and 2-D crystals. For samples other than those for monolayer crystallization experiments, typically a 5-μl aliquot was placed on a glow-discharged (hydrophilic) 300-mesh copper EM grid covered by a plastic-supported continuous carbon film. After 90 seconds, the sample was washed three times with deionized water and stained with 1.5% uranyl acetate for 1 min. Excess solution was then blotted with a piece of filter paper, and the grid was allowed to air dry. In the case of investigations with lipid monolayer crystals, following staining and air drying, the grid was coated with a thin film of evaporated carbon. EM grids were examined in a Philips Tecnai 12 electron microscope operated at 120 kV in a low-dose mode. Images were recorded on SO-163 film (Kodak) at a nominal magnification of ×42,000 and a 0.8- to 1.0-μm underfocus and were developed for 11 min in D19 (Kodak) diluted 1:1 with deionized water. The images of tilted crystals (up to ±55°) were recorded at approximately 10° increments in a tilt series starting with the nominally untilted view. The cumulative dose for the tilt series was estimated to be ~200 e/Å^2. Micrographs were examined in an optical diffractometer to assess levels of defocus, drift, and astigmatism and to select the best-ordered regions of a crystal. Using a Leafscan 45 scanner (Leaf Systems Inc.), these selected areas of the micrographs, typically 5 cm by 6 cm, were digitized at 2,540 dpi, corresponding to a sampling at approximately 2.4 Å on the specimen.

Image processing. Digitized areas of 2,048 by 2,048 pixels from 25 micrographs of type I crystals belonging to three tilt series were selected. The images were processed by using the MRC program suite for 2-D crystallography (11, 19). Nominally untilted images were used to determine the unit cell dimensions of the crystal lattice. Amplitudes and phases sampled along the lattice lines were extracted after subjecting the tilt series images usually to two rounds of the lattice "unbending" procedure, to minimize the effects of lattice distortion. The tilt geometry was determined from the foreshortening of the unit cell dimensions and from the changes in defocus across the tilt axis in the micrograph. The absolute sign of the tilt angle was determined by noting which side of the micrograph was more underfocused, indicating that this part of the crystal was at a lower *z* height in the microscope (3). At the defocus used (0.8 to 1.0 μm), the highest-resolution spot was located within the first node of the contrast transfer function, and thus no correction for phase reversal was applied. The extracted phases and amplitudes for each untilted image were subjected to the program ALLSPACE (19) to determine which of the 17 possible two-sided plane groups of symmetry represented the best fit. In this exercise, the values of the phases of significant spots in the computed diffraction pattern were checked to query the lattice symmetry based on the calculated phase residuals. The 'best' untilted image with the smallest phase residual as determined by ALLSPACE was used as the reference to bring the images of tilted views to a common phase origin using the program ORIGTILTK. First, based on the geometry of the tilt (i.e., the tilt angle and its orientation in the image), the reciprocal lattice z^* coordinate of all the reflections in the computed diffraction pattern of an image of the tilted crystal was calculated. For a given image, the phase origin was determined such that the shifted values of the phases for the various reflections yielded the lowest residuals compared with those for the same reflections from other images. For this purpose, values of the phases sampled for a given reflection along a lattice line that were within $\Delta z^* = 1/120$ Å^{-1}, corresponding to an approximate vertical thickness of 120 Å for orfv075, were deemed to be equivalent and compared in the phase origin search. The merged phases and amplitudes along the various lattice lines were least-squares fitted using LATLINEA (19) and plotted as a

function of $z*$. The phase and amplitude profiles for each reflection were regularly sampled using an arbitrary unit cell dimension (200 Å) along the z axis, and a 3-D density map was calculated by reverse Fourier transformation of the sampled structure factor amplitudes and phases. The map was displayed using PyMOL (version 0.98; DeLano Scientific LLC).

Predictive analysis based on the amino acid sequence. The amino acid sequences of orfv075 (ORFV strain NZ2) (30) and its orthologue D13 (vaccinia virus Copenhagen strain) (16) were used for predictive analysis. An initial amino acid sequence-based homologue search was performed by PSI-BLAST (2). Major elements of secondary structure (e.g., α-helix and β-sheet) in orfv075 and D13 were assessed by PSIPRED (23). orfv075 homologues with known 3-D structures were identified by sequence alignment/secondary structure prediction-based search using the Phyre (25) and the HHpred (45) servers.

Fitting of atomic structures of orfv075 homologues into the EM-derived 3-D density map. Using PyMOL, the X-ray structures were docked into the "tripod" region of the density map where visually maximal overlaps could be seen. The fit was then optimized using the program URO (39), based first on the whole density map and subsequently on only the matching region. To excise this region of the map, a mask was created based on the X-ray structure of one of the homologues as a template, using a probe radius of 5 Å, and the extent of the mask was further inflated isotropically by 4 Å. Cross correlation between the volume of the orfv075 density map enclosed by the mask and the individual X-ray structures was calculated by comparison of the complex structure factors.

Ultrathin section EM of ORFV-infected cells. Primary lamb testis cells at 14 hours postinfection by ORFV (NZ2 strain) were pelleted and fixed in 2% glutaraldehyde in 0.15 M cacodylate buffer, pH 8.0, for 1 h. After three 5-minute washes with the fixing buffer, cells were treated with 2% OsO_4 in 0.15 M cacodylate buffer, pH 6.9, for 2 h at room temperature, washed three times as before, and resuspended in low-melting-point agarose. After the agarose had set, the block was cut into 1-mm^3 pieces and treated with 1.5% potassium ferricyanide and 1% OsO_4 in 0.15 M cacodylate buffer, pH 8.0, for 1 h to enhance membrane contrast. Three further washes in the fixing buffer were followed by staining with 1% uranyl acetate for 1 h at room temperature and by three washes with distilled water. Samples were then dehydrated through an ethanol series (70%, 95%, and 100% ethanol; 10 min each) and embedded in Quetol 651 resin. Sections of ~80 nm were poststained with uranyl acetate and lead citrate, and images were acquired using a Philips CM12 TEM operated at 120 kV.

RESULTS

We used recombinant orfv075 produced in *E. coli* for biochemical and structural characterization of this putative ORFV scaffolding protein.

Biochemical characterization of orfv075. SEC showed that a majority of the protein elutes in the void volume, where species with molecular masses of greater than ~600 kDa migrate. Upon removal of the N-terminal His tag with the rTEV protease, orfv075 eluted at a position compatible with a trimer. Sodium dodecyl sulfate-polyacrylamide gel electrophoresis (SDS-PAGE) demonstrated that oligomerized or aggregated orfv075 in the void-volume fraction as well as the protein trimers are essentially pure (Fig. 1). These results showed (i) that orfv075 organizes as a trimer and (ii) that the aggregation of orfv075 trimers is promoted by the presence of the N-terminal His tag. However, under appropriate conditions, the His-tagged protein could self-assemble into ordered arrays in situ, and the His tag was directly exploited to allow interaction with functionalized lipids for 2-D crystallization experiments on lipid monolayers. Therefore, the interactions involved in the observed aggregation are very likely weak and reversible.

EM of negatively stained His-tagged orfv075 revealed heterogeneous tubular objects and small patches of honeycomb-shaped crystals over a background of small globular protein oligomers (diameter, ~6 nm) (Fig. 2). These small crystalline patches, with a ~14-nm hexagonal lattice spacing, were formally similar to those described for the D13 vaccinia virus
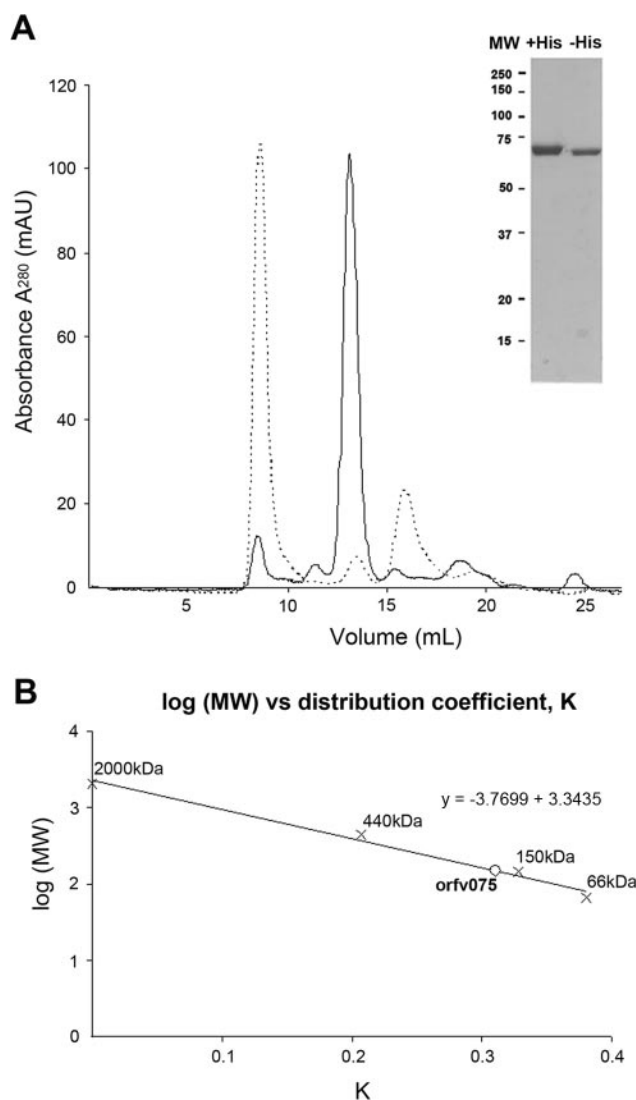

FIG. 1. SEC of orfv075 with or without a His tag and estimation of molecular mass of His tag-cleaved orfv075. (A) The majority of the His-tagged orfv075 (chromatogram with dashed line), purified by immobilized metal affinity chromatography, exists as aggregates eluting in the void volume. Upon cleavage of the His tag by rTEV protease, the majority of protein sample (chromatogram with solid line) dissociates into smaller oligomers. In both cases, the protein is essentially pure as indicated by the ~65-kDa (+His tag) or ~60-kDa (−His tag) bands in SDS-PAGE (inset). (B) Log values of molecular mass of standards are plotted as a function of distribution coefficients, K, in order to estimate the molecular mass of the eluent from gel filtration. Based on the elution volume of His tag-cleaved orfv075 in the gel filtration chromatogram, the molecular mass was estimated to be ~160 kDa, indicated by a circle. Assuming that a nonglobular shape of oligomeric orfv075 is hampering precise measurement, the estimated molecular mass would correspond to homotrimers of orfv075.

orthologue of orfv075 (47) but did not extend to sizeable 2-D crystals.

Analysis of orfv075 2-D crystals. One of the experiments designed to test for improvement in the homogeneity of His-tagged orfv075 involved exchange of the buffer from 50 mM to 10 mM Tris. This buffer exchange appeared to induce orfv075 to spontaneously form 2-D crystals (type I crystal)
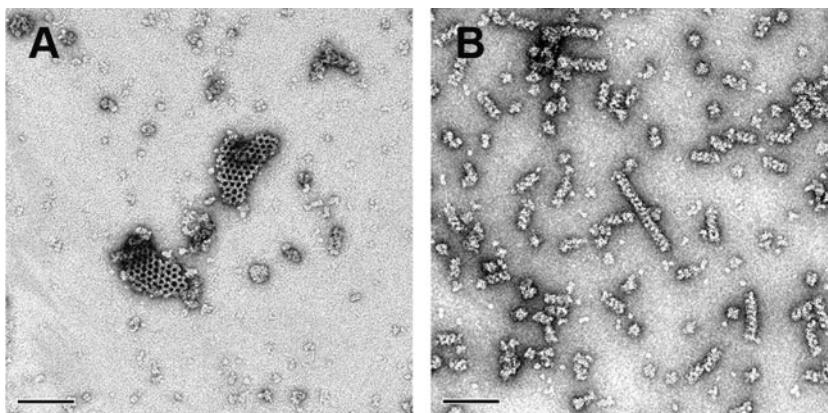
FIG. 2. The purified His-tagged orfv075 oligomers exhibit variable morphologies as visualized from specimens preserved in negative stain. Aggregates of honeycomb-shaped crystalline patches (A) and tubular objects with heterogeneous length (B) are observed. The background consists of smaller protein oligomers. The images were recorded using a BIOSCAN charge-coupled device camera. Bars, 100 nm.

(Fig. 3A). These crystals sometimes extended up to 3 μm in length. On the other hand, in comparison, the 2-D crystals grown on lipid monolayer (type II crystal) (Fig. 3B) were considerably smaller (average length of ~0.5 μm). These crystals appeared fragile, especially during transfer to continuous carbon-coated EM grids, and necessitated the use of holey carbon films that were postcoated with carbon to stabilize the specimen under the electron beam.

The type I crystal has lattice dimensions of $a = b = 140$ Å ($\pm$ 3Å), and based on the analysis of the phase residuals (Table 1) (see Materials and Methods), the plane group of symmetry is p3, indicating the presence of threefold symmetry. The p3 symmetry was confirmed in a projection map (Fig. 4A) calculated without imposing the symmetry where compact trimeric subunits could be clearly identified. The continuous array of trimers does not display significant intertrimer interactions, with the region between the trimers being largely permeated by stain. This differs from the dense hexagonal packing charac-

terizing the small crystalline patches seen in purified orfv075 samples or in the D13 scaffold covering vaccinia virus IV. On the other hand, the morphology of type II crystals formally appeared to be similar to that of the honeycomb scaffold of D13. A projection density map for the type II crystal confirmed a denser packing of the orfv075 trimers characterized by the p6 plane group of symmetry (Table 1), with unit cell dimensions of $a = b = 154$ Å ($\pm$ 4Å) (Fig. 4B).

3-D model of orfv075. Our efforts in 3-D reconstruction using images of tilted crystals focused primarily on the type I crystals because of their superior quality. Data up to a maximum resolution of 25 Å were included in the calculation of the density map as shown by the extracted amplitudes and phases plotted along the lattice lines (Fig. 5).

A surface representation of the orfv075 trimer is shown in Fig. 6, thresholded such that the model has a volume corresponding to a trimer with a molecular mass of 195 kDa (3 × 65 kDa; protein partial specific volume = 1.35). At the modest
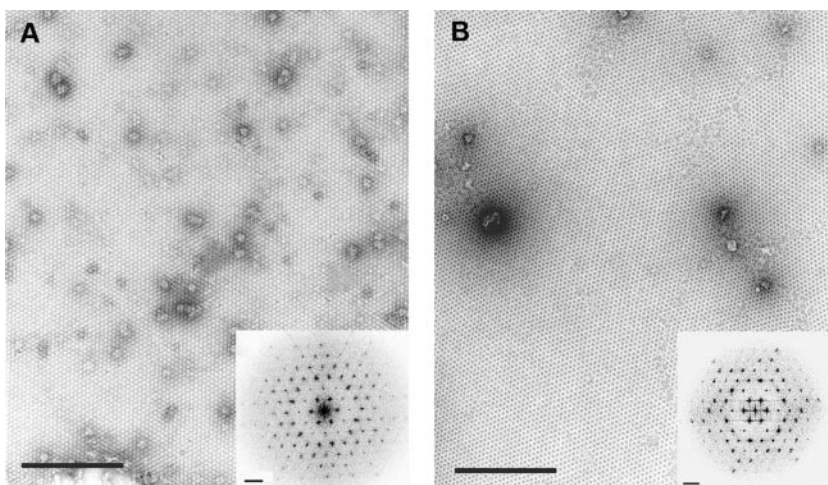

FIG. 3. Negatively stained 2-D crystals of recombinant His-tagged orfv075. (A) Crystals produced in situ (type I crystals). (B) Crystals produced on lipid monolayer (type II crystals). Relatively large aggregates overlay both crystal types. The type II crystals often showed discontinuity, possibly due to mechanical stress upon transfer from the air-water interface. The insets show computed Fourier transforms of sections of crystals that exhibit hexagonal symmetry. Reflections up to resolutions of 18 Å and 20 Å are visible for type I and type II crystals, respectively. Bars, 200 nm in the micrographs and 200 Å^{-1} in the computed diffractograms.

TABLE 1. Statistics of analysis of plane group of symmetry of orfv075 2-D crystal lattices[a]

Crystal type	Two-sided plane group of symmetry	Phase residual vs other spots (90° random)	No. of comparisons	Target residual based on statistics taking Friedel wt into account
I	p1	15.8	154	
	p2	58.1	77	22.6
	c12_b	55.9	49	16.5
	c12_a	60.1	50	16.6
	p3	16.7[b]	138	15.8
	p312	53.9	329	16.0
	p321	23.5[c]	334	16.1
	p6	40.6	353	17.3
	p622	54.5	740	16.5
II	p1	18.9	124	
	p2	17.5[b]	62	27.7
	c12_b	68.0	46	19.6
	c12_a	76.7	46	19.6
	p3	10.9[b]	98	18.9
	p312	39.7	243	19.1
	p321	39.1	247	19.2
	p6	11.3[b]	258	20.8
	p622	36.4	552	19.8

[a] Results from the ALLSPACE program (as described in Materials and Methods) that established the plane group of symmetry of orfv075 2-D crystals. Reflections in the computed diffraction pattern of a nominally untilted 2-D crystal whose background-corrected amplitudes were equal to or greater than one standard deviation in the background were included in the analysis. The correct symmetry corresponds to that with the lowest phase residual for 1 of the 9 (out of 17) possible two-sided plane groups of symmetry consistent with the lattice geometry. The values of the calculated residuals indicate p3 (threefold) and p6 plane (sixfold) groups of symmetry for type I and type II crystals, respectively. The higher symmetry, p6, was assigned to the type II crystal, as the residuals for p3 and p6 are statistically indistinguishable.
[b] Acceptable choice for the plane group of symmetry.
[c] Possible choice for the plane group of symmetry.

25-Å resolution it is not possible to unambiguously define the monomer boundary. The height of the barrel-shaped orfv075 trimer is ~90 Å, with a diameter of ~70 Å. The orientation of the orfv075 was arbitrarily decided so that the trimer volume could be characterized by two domains: a "propeller" head and a relatively larger "tripod" base. There is a large cavity circumscribed by the "legs" of the tripod, and a small protrusion extends from the top of the propeller domain around the threefold axis. The trimers are approximately 55 Å apart in the crystal. The absence of a visible connection between the tri-

mers is probably an artifact caused by insufficient resolution and preferential permeation of stain.

Based on preliminary tilt series data recorded from type II crystals, a 3-D reconstruction was also generated. Although inferior in resolution and quality, the overall features of the orfv075 trimer (e.g., the tripod-like base) were similar to those seen in the reconstruction from type I crystals (data not shown). More interestingly, based on this reconstruction, the orientation of the trimer with respect to the lipid monolayer could be directly deduced by virtue of the fact that the type II
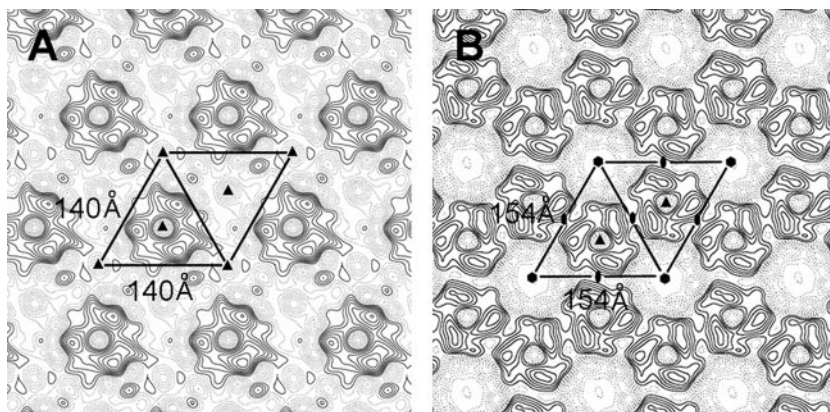

FIG. 4. Projection density maps calculated from images of nominally untilted recombinant orfv075 2-D crystals. No symmetry was imposed, and one unit cell is demarcated. Positive and negative densities, represented by continuous and dashed contour lines, denote, respectively, regions of protein and stain. (A) Type I crystal. Compact trimeric subunits arranged with p3 symmetry are clearly visible. Regions between the trimers are extensively permeated by stain. The unit cell edge is $a = b = 140$ Å. (B) Type II crystal. Compact trimeric subunits arranged with p6 symmetry exhibit denser crystal packing. Six adjacent trimers surround large stain-filled channels in the crystal. The unit cell dimensions are $a = b = 154$ Å.
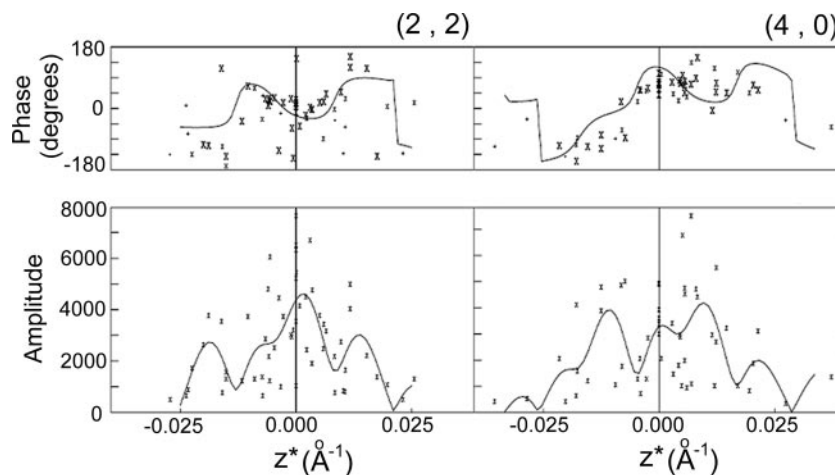
FIG. 5. Phase and amplitude variations as a function of reciprocal lattice coordinate z^* generated from tilted type I crystals and analyzed with the p3 plane group of symmetry. Phase and amplitude profiles for two example lattice lines (2,2 and 4,0) are shown. The least-squares-fitted profiles were regularly sampled at intervals of 0.005 Å^{-1} to yield 3-D structure factors. Data to a maximum resolution of ~25 Å were used in the reconstruction.

crystal formation is induced by the interaction of the His tag located at the N terminus of the protein with the nickel-chelating lipid. In the reconstructed 3-D model, the tripod domain is proximal to the lipid monolayer, with the propeller domain distal from the monolayer. This indicates that the N terminus of orfv075 is located at the base of the tripod domain.

Sequence and structure comparisons. A PSI-BLAST search identified NCLDV homologues of orfv075, including the major capsid proteins of iridovirus, mimivirus, and ascorvirus, whereas the major capsid protein of phycodnavirus was also found when the amino acid sequence of D13 was used. This is in line with results obtained by Iyer and colleagues (21).

Analysis by the PSIPRED server predicted that orfv075 is composed of 27% β-strands and 17.6% α-helices. Although within the poxvirus family there are no orthologues of orfv075 with known structure, we searched for distant homologues using HHpred. The best match was the capsid protein VP54 (PDB-ID 1J5Q) (38) of *Paramecium bursaria Chlorella* virus type 1 (PBCV-1) over 193 aligned residues (15% sequence identity), with 82.8% probability and an E value of 0.021. VP54 is composed of two parallel N- and C-terminal jelly roll domains and assembles as trimers. In these trimers, the six jelly rolls display similar dispositions, resulting in a pseudohexamer.

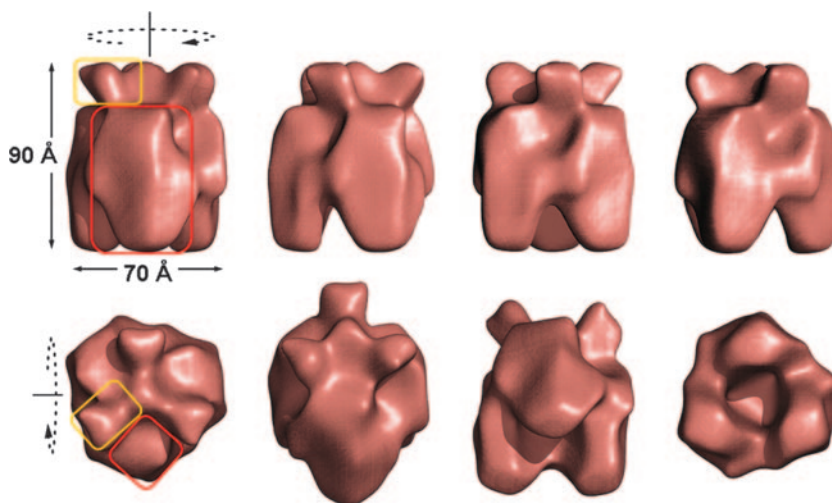Docking of the atomic model of VP54 into the 3-D density

FIG. 6. A montage of different views of the surface-rendered 3-D density volume of the recombinant orfv075 trimer generated from analysis of images of type I crystals. The 3-D reconstruction at a resolution of ~25 Å was computed using images of tilted negatively stained crystals. The top row shows views of the model rotated around the axis of threefold symmetry, and the bottom row shows views of the model rotated around an arbitrary axis perpendicular to threefold symmetry and includes views along the threefold from the "top" (far left) and from the "bottom" (far right) of the orfv075 trimer. The trimer (~90 Å in height by ~70 Å wide) is composed of a small "propeller" domain connected to a larger "tripod" base, designated in orange (propeller domain) and in red (tripod base) apportioned arbitrarily for one monomer. The "legs" of the tripod base surround a deep cavity that appears to be bounded by a small protrusion in the propeller domain. The density threshold (= 1.3σ) is appropriate for the expected volume of the trimer.
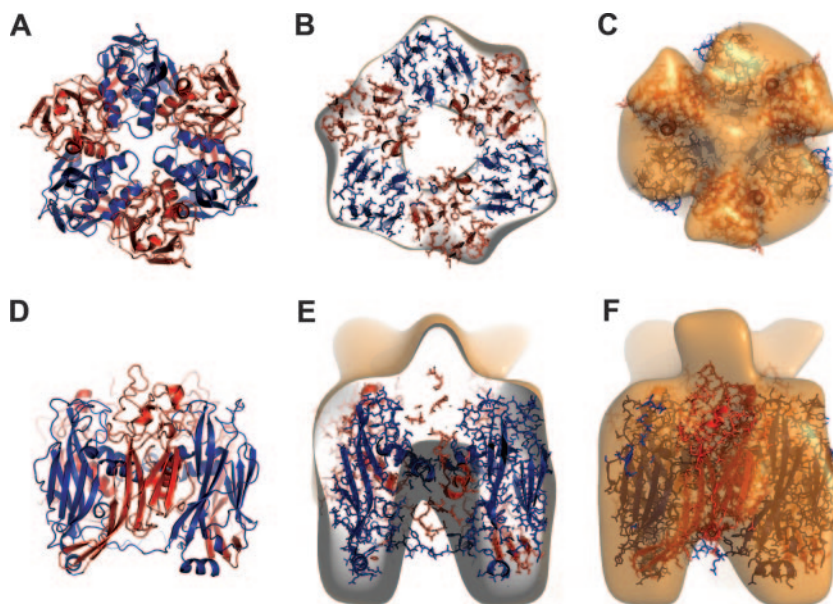
FIG. 7. Docking of VP54 of PBCV-1 into the 3-D model of orfv075 trimer. The top and bottom panels represent views, respectively, down and normal to the threefold axis of the trimer of PBCV-1 VP54 (A and D). The atomic structure of VP54 is represented as a cartoon with the N- and C-terminal jelly roll domains in blue and red, respectively. (B and E) The fit of the VP54 trimer into the 3-D model of orfv075 is shown as a composite of the docked X-ray structure and a surface-rendered (1.3 σ) view of orfv075 cutting through approximately the center of the model. (C and F) Similar views of the whole model.

map of orfv075 revealed a surprisingly good agreement with the "tripod" domain. The agreement cross correlation at 25-Å resolution was 0.85. The masked volume of orfv075 used in the cross correlation calculations (see Materials and Methods) included the whole of the orfv075 density envelope except the extremity of the "propeller" domain. In this orientation, the N terminus of VP54 is at the base of the tripod, which is compatible with the deduced location of the N-terminal His tag of orfv075 as described above. Although the reconstructed density map of orfv075 is not markedly pseudohexameric, the VP54 trimer fits nicely in the molecular envelope of the tripod domain, with the two jelly rolls flanked by helices and loops occupying a leg of the tripod (Fig. 7). The propeller-like domain of the orfv075 trimer, however, did not have a corresponding domain in VP54. This could be due to the presence of larger loops in orfv075, as orfv075 has 545 amino acid residues, compared to 437 residues for VP54.

We also examined the fit of the atomic structures of the major capsid proteins of bacteriophage PRD-1 (PDB-ID 1CJD) (7) and *Sulfolobus* turreted icosahedral virus (PDB-ID 2BBD) (26), as well as the adenovirus hexon protein (PDB-ID 1P30) (42). The major capsid proteins of PRD-1 and *Sulfolobus* turreted icosahedral virus display a similar fit with the orfv075 density map (cross correlation of 0.81) as in the case of VP54. Whereas VP54 has loops protruding into the propeller domain of orfv075, these proteins are smaller and lack any corresponding volume for the propeller domain. On the other hand, the adenovirus hexon (951 residues) is too large to fit into the orfv075 molecular envelope and also possesses extra loops with no equivalents in orfv075. Overall, there is good correspondence of the double-barrel "base" of these capsid proteins into our structure of orfv075.

DISCUSSION

orfv075 is the orthologue of the protein D13 of vaccinia virus (57% sequence identity), which is also called the rifampin resistance gene product (37). A number of studies have identified amino acid residues that confer rifampin resistance (5, 9, 29). Interestingly, some of the substituted amino acid residues in rifampin-resistant D13 mutants are the same as those at analogous positions in the orfv075 sequence. This is consistent with our finding that ORFV is naturally resistant to rifampin (data not shown). On the other hand, the high sequence conservation of this gene product indicates that the critical role of D13 in the assembly of vaccinia virus immature particles is probably shared by all D13 orthologues. In fixed thin sections of primary lamb testis cells, at ~14 h postinfection by ORFV, we could detect objects that are reminiscent of crescents that were identified in vaccinia virus-infected cells, suggesting that parapoxviruses follow an assembly path similar to that of orthopoxviruses (Fig. 8). In vivo, D13 can organize on membrane segments of IV (13) and can also self-assemble in so-called honeycomb lattices (20, 47).

We pursued structural studies of recombinant orfv075 with the goal of understanding the structure/function correlates of orfv075. We found that orfv075 can spontaneously assemble to form 2-D crystals (type I) that turned out to be of better quality than 2-D crystals obtained on functionalized lipid monolayers (type II). We note that planar crystals of D13 (similar to type II) were seen only in vivo when a single point mutation, D513G, was introduced (47). Interestingly, the observed ability of orfv075 to self-associate in vitro into ordered arrays in the absence of other viral proteins is analogous to that displayed by many capsid proteins.
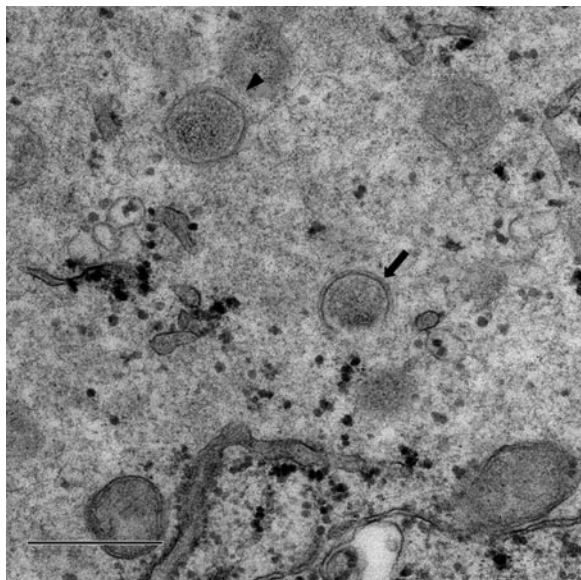
FIG. 8. View of thin section of cytoplasm of an ORFV-infected cell at 14 h postinfection. The cells were fixed and embedded in Quetol 651 resin prior to ultrathin sectioning. The arrowhead indicates a spherical structure that resembles IV of vaccinia virus and encloses dense regions possibly representing condensed viral proteins and DNA. The arrow indicates an incomplete spherical object similar to the crescent-shaped precursor of IV. An extra layer on the outer surface of these structures is apparent, suggestive of orfv075 scaffolding analogous to D13 lattice on vaccinia virus IV. Bar, 0.5 μm.

The structure of orfv075 presented here and the docking of VP54 capsid protein suggest that orfv075 is composed of two consecutive jelly roll domains occupying the tripod-like base and protruding loops forming the propeller-like head of the trimer. This tentative fold for orfv075 is supported by secondary structure predictions as well as the observation of a degradation product in protein expressed at temperatures higher than 20°C. This proteolytic fragment has an approximate molecular mass of 30 kDa (estimated from SDS-PAGE) and belongs to an N-terminal domain of orfv075 as identified by mass spectrometry of trypsin-digested orfv075 (data not shown). This is consistent with a cleavage in a linker between the two putative jelly roll domains in orfv075. The cleavage of capsid protein by viral proteases has been shown to be essential to trigger the complex process of maturation of IV into infectious IMV. It will be interesting to investigate the involvement of proteolytic processing of orfv075 in the viral maturation.

Poxviruses have been postulated to be a member of a large family of viruses called NCLDV. Vaccinia virus D13, and presumably its orthologue orfv075, is essential in viral morphogenesis and belongs in the basic set of proteins shared by all the NCLDV (21, 22). Interestingly, all other members of the NCLDV display icosahedral symmetry, and some of the homologues of D13 have been shown to be part of the icosahedral shell (49). All the known structures of these trimeric capsid proteins harbor a similar double-barrel fold proposed to be characteristic of an ancient viral lineage spanning all domains of life (6). The good fit of the trimer of VP54 of PBCV-1 in the molecular envelope of orv075 together with the evolutionary link postulated from sequence analysis supports the inclusion of poxviruses in this viral lineage. Poxvirus could thus be the first member of this lineage with an infectious virion lacking icosahedral symmetry.

Recent studies on D13 have shown that the N- and C-terminal ends of the protein are involved in resistance to rifampin, suggesting that these regions could come together to form a rifampin-binding site. The model of orfv075 proposed here supports this view. Based on the fit of VP54 in the map, orfv075 would have both its N and C termini located at the bottom of the tripod domain. These regions could be involved in interaction with integral membrane viral proteins similar to that seen for another NCLDV, PRD1. Interaction of the protein P3 of PRD1 with membrane-bound proteins through the N-terminal tail is indeed observed in the structure of icosahedral PRD1 virus particles (1). The preliminary reconstruction based on the data from type II crystals suggests that the tripod base of the orfv075 trimer is in contact with the membrane surface while the propeller domain is distal from the membrane and that the trimers are held together by intimate lateral packing. This largely reflects the organization found in PRD1, where the counterpart of the tripod domain is involved in binding to the internal proteins and membrane, the lateral faces of the trimer ensure the formation of the icosahedral shell, and loops from both jelly rolls protrude from the surface of the virus (1). More detailed structure-based comparisons between poxvirus IV and membrane-containing icosahedral viruses could bring new insights into the assembly of poxvirus.

REFERENCES

1. **Abrescia, N. G., J. J. Cockburn, J. M. Grimes, G. C. Sutton, J. M. Diprose, S. J. Butcher, S. D. Fuller, C. San Martin, R. M. Burnett, D. I. Stuart, D. H. Bamford, and J. K. Bamford.** 2004. Insights into assembly from structural analysis of bacteriophage PRD1. Nature **432:**68–74.
2. **Altschul, S. F., T. L. Madden, A. A. Schaffer, J. Zhang, Z. Zhang, W. Miller, and D. J. Lipman.** 1997. Gapped BLAST and PSI-BLAST: a new generation of protein database search programs. Nucleic Acids Res. **25:**3389–3402.
3. **Amos, L. A., R. Henderson, and P. N. Unwin.** 1982. Three-dimensional structure determination by electron microscopy of two-dimensional crystals. Prog. Biophys. Mol. Biol. **39:**183–231.
4. **Andrews, P.** 1962. Estimation of molecular weights of proteins by gel filtration. Nature **196:**36–39.
5. **Baldick, C. J., Jr., and B. Moss.** 1987. Resistance of vaccinia virus to rifampicin conferred by a single nucleotide substitution near the predicted NH2 terminus of a gene encoding an Mr 62,000 polypeptide. Virology **156:**138–145.
6. **Bamford, D. H., J. M. Grimes, and D. I. Stuart.** 2005. What does structure tell us about virus evolution? Curr. Opin. Struct. Biol. **15:**655–663.
7. **Benson, S. D., J. K. Bamford, D. H. Bamford, and R. M. Burnett.** 1999. Viral evolution revealed by bacteriophage PRD1 and human adenovirus coat protein structures. Cell **98:**825–833.
8. **Betakova, T., E. J. Wolffe, and B. Moss.** 1999. Regulation of vaccinia virus morphogenesis: phosphorylation of the A14L and A17L membrane proteins and C-terminal truncation of the A17L protein are dependent on the F10L kinase. J. Virol. **73:**3534–3543.
9. **Charity, J. C., E. Katz, and B. Moss.** 2007. Amino acid substitutions at multiple sites within the vaccinia virus D13 scaffold protein confer resistance to rifampicin. Virology **359:**227–232.
10. **Condit, R. C., N. Moussatche, and P. Traktman.** 2006. In a nutshell: structure and assembly of the vaccinia virion. Adv. Virus Res. **66:**31–124.
11. **Crowther, R. A., R. Henderson, and J. M. Smith.** 1996. MRC image processing programs. J. Struct. Biol **116:**9–16.

12. **Cyrklaff, M., C. Risco, J. J. Fernandez, M. V. Jimenez, M. Esteban, W. Baumeister, and J. L. Carrascosa.** 2005. Cryo-electron tomography of vaccinia virus. Proc. Natl. Acad. Sci. USA **102:**2772–2777.

13. **Dales, S., and E. H. Mosbach.** 1968. Vaccinia as a model for membrane biogenesis. Virology **35:**564–583.

14. **Delhon, G., E. R. Tulman, C. L. Afonso, Z. Lu, A. de la Concha-Bermejillo, H. D. Lehmkuhl, M. E. Piccone, G. F. Kutish, and D. L. Rock.** 2004. Genomes of the parapoxviruses ORF virus and bovine papular stomatitis virus. J. Virol. **78:**168–177.

15. **Essani, K., R. Dugre, and S. Dales.** 1982. Biogenesis of vaccinia: involvement of spicules of the envelope during virion assembly examined by means of conditional lethal mutants and serology. Virology **118:**279–292.

16. **Goebel, S. J., G. P. Johnson, M. E. Perkus, S. W. Davis, J. P. Winslow, and E. Paoletti.** 1990. The complete DNA sequence of vaccinia virus. Virology **179:**247–266, 517–563.

17. **Haig, D. M.** 2006. Orf virus infection and host immunity. Curr. Opin. Infect. Dis. **19:**127–131.

18. **Haig, D. M., and A. A. Mercer.** 1998. Ovine diseases. Orf. Vet. Res. **29:**311–326.

19. **Henderson, R., J. M. Baldwin, T. A. Ceska, F. Zemlin, E. Beckmann, and K. H. Downing.** 1990. Model for the structure of bacteriorhodopsin based on high-resolution electron cryo-microscopy. J. Mol. Biol. **213:**899–929.

20. **Heuser, J.** 2005. Deep-etch EM reveals that the early poxvirus envelope is a single membrane bilayer stabilized by a geodetic "honeycomb" surface coat. J. Cell Biol. **169:**269–283.

21. **Iyer, L. M., L. Aravind, and E. V. Koonin.** 2001. Common origin of four diverse families of large eukaryotic DNA viruses. J. Virol. **75:**11720–11734.

22. **Iyer, L. M., S. Balaji, E. V. Koonin, and L. Aravind.** 2006. Evolutionary genomics of nucleo-cytoplasmic large DNA viruses. Virus Res. **117:**156–184.

23. **Jones, D. T.** 1999. Protein secondary structure prediction based on position-specific scoring matrices. J. Mol. Biol. **292:**195–202.

24. **Katz, E., and B. Moss.** 1970. Vaccinia virus structural polypeptide derived from a high-molecular-weight precursor: formation and integration into virus particles. J. Virol. **6:**717–726.

25. **Kelley, L. A., R. M. MacCallum, and M. J. Sternberg.** 2000. Enhanced genome annotation using structural profiles in the program 3D-PSSM. J. Mol. Biol. **299:**499–520.

26. **Khayat, R., L. Tang, E. T. Larson, C. M. Lawrence, M. Young, and J. E. Johnson.** 2005. Structure of an archaeal virus capsid protein reveals a common ancestry to eukaryotic and bacterial viruses. Proc. Natl. Acad. Sci. USA **102:**18944–18949.

27. **Lévy, D., G. Mosser, O. Lambert, G. S. Moeck, D. Bald, and J. L. Rigaud.** 1999. Two-dimensional crystallization on lipid layer: a successful approach for membrane proteins. J. Struct. Biol **127:**44–52.

28. **Malkin, A. J., A. McPherson, and P. D. Gershon.** 2003. Structure of intracellular mature vaccinia virus visualized by in situ atomic force microscopy. J. Virol. **77:**6332–6340.

29. **McNulty-Kowalczyk, A., and E. Paoletti.** 1993. Mutations in ORF D13L and other genetic loci alter the rifampicin phenotype of vaccinia virus. Virology **194:**638–646.

30. **Mercer, A. A., N. Ueda, S. M. Friederichs, K. Hofmann, K. M. Fraser, T. Bateman, and S. B. Fleming.** 2006. Comparative analysis of genome sequences of three isolates of Orf virus reveals unexpected sequence variation. Virus Res. **116:**146–158.

31. **Mercer, J., and P. Traktman.** 2005. Genetic and cell biological characterization of the vaccinia virus A30 and G7 phosphoproteins. J. Virol. **79:**7146–7161.

32. **Miner, J. N., and D. E. Hruby.** 1989. Rifampicin prevents virosome localization of L65, an essential vaccinia virus polypeptide. Virology **170:**227–237.

33. **Mohandas, A. R., and S. Dales.** 1995. Involvement of spicules in the formation of vaccinia virus envelopes elucidated by a conditional lethal mutant. Virology **214:**494–502.

34. **Moss, B.** 2001. Poxviridae: the viruses and their replication, p. 2849–2883. *In* B. N. Fields, D. M. Knipe, and P. M. Howley (ed.), Fields virology, 4th ed. Lippincott Williams and Wilkins, Philadelphia, PA.

35. **Moss, B.** 2006. Poxvirus entry and membrane fusion. Virology **344:**48–54.

36. **Moss, B., E. N. Rosenblum, and P. M. Grimley.** 1971. Assembly of vaccinia virus particles from polypeptides made in the presence of rifampicin. Virology **45:**123–134.

37. **Moss, B., E. N. Rosenblum, E. Katz, and P. M. Grimley.** 1969. Rifampicin: a specific inhibitor of vaccinia virus assembly. Nature **224:**1280–1284.

38. **Nandhagopal, N., A. A. Simpson, J. R. Gurnon, X. Yan, T. S. Baker, M. V. Graves, J. L. Van Etten, and M. G. Rossmann.** 2002. The structure and evolution of the major capsid protein of a large, lipid-containing DNA virus. Proc. Natl. Acad. Sci. USA **99:**14758–14763.

39. **Navaza, J., J. Lepault, F. A. Rey, C. Alvarez-Rua, and J. Borge.** 2002. On the fitting of model electron densities into EM reconstructions: a reciprocal-space formulation. Acta Crystallogr. D **58:**1820–1825.

40. **Risco, C., J. R. Rodriguez, C. Lopez-Iglesias, J. L. Carrascosa, M. Esteban, and D. Rodriguez.** 2002. Endoplasmic reticulum-Golgi intermediate compartment membranes and vimentin filaments participate in vaccinia virus assembly. J. Virol. **76:**1839–1855.

41. **Rosel, J., and B. Moss.** 1985. Transcriptional and translational mapping and nucleotide sequence analysis of a vaccinia virus gene encoding the precursor of the major core polypeptide 4b. J. Virol. **56:**830–838.

42. **Rux, J. J., P. R. Kuser, and R. M. Burnett.** 2003. Structural and phylogenetic analysis of adenovirus hexons by use of high-resolution X-ray crystallographic, molecular modeling, and sequence-based methods. J. Virol. **77:**9553–9566.

43. **Smith, G. L., A. Vanderplasschen, and M. Law.** 2002. The formation and function of extracellular enveloped vaccinia virus. J. Gen. Virol. **83:**2915–2931.

44. **Sodeik, B., R. W. Doms, M. Ericsson, G. Hiller, C. E. Machamer, W. van't Hof, G. van Meer, B. Moss, and G. Griffiths.** 1993. Assembly of vaccinia virus: role of the intermediate compartment between the endoplasmic reticulum and the Golgi stacks. J. Cell Biol. **121:**521–541.

45. **Soding, J., A. Biegert, and A. N. Lupas.** 2005. The HHpred interactive server for protein homology detection and structure prediction. Nucleic Acids Res. **33:**W244–W248.

46. **Spehner, D., S. De Carlo, R. Drillien, F. Weiland, K. Mildner, D. Hanau, and H. J. Rziha.** 2004. Appearance of the bona fide spiral tubule of ORF virus is dependent on an intact 10-kilodalton viral protein. J. Virol. **78:**8085–8093.

47. **Szajner, P., A. S. Weisberg, J. Lebowitz, J. Heuser, and B. Moss.** 2005. External scaffold of spherical immature poxvirus particles is made of protein trimers, forming a honeycomb lattice. J. Cell Biol. **170:**971–981.

48. **Tolonen, N., L. Doglio, S. Schleich, and J. Krijnse Locker.** 2001. Vaccinia virus DNA replication occurs in endoplasmic reticulum-enclosed cytoplasmic mini-nuclei. Mol. Biol. Cell **12:**2031–2046.

49. **Yan, X., N. H. Olson, J. L. Van Etten, M. Bergoin, M. G. Rossmann, and T. S. Baker.** 2000. Structure and assembly of large lipid-containing dsDNA viruses. Nat. Struct. Biol. **7:**101–103.

50. **Zhang, Y., and B. Moss.** 1992. Immature viral envelope formation is interrupted at the same stage by lac operator-mediated repression of the vaccinia virus D13L gene and by the drug rifampicin. Virology **187:**643–653.